

Estimation of woodland canopy structure with terrestrial LiDAR: extended methods

John L. Godlee

22nd August 2021

1 1 Introduction

This chapter provides expanded field and analytical methods for the study of tree canopy structure in southern African woodlands, presented in brief in Chapter 5. The study aimed to understand the effects of tree species diversity and stand structure on tree canopy structural complexity, using terrestrial LiDAR. Firstly, I provide technical details on the field setup for the terrestrial LiDAR and the hemispherical photography used to validate terrestrial LiDAR canopy closure estimates. Secondly, I describe the processing chain used to extract canopy complexity metrics from the terrestrial LiDAR point clouds. Thirdly, I describe in further detail the behaviour and suitability of the different canopy complexity and stand structural metrics used in the study.

11 2 Terrestrial LIDAR field setup

Within each 1 ha (100×100 m) square plot, nine 10 m diameter circular subplots were laid out in a grid, with 35 m between subplot centre points (Figure 1). These subplots constitute the basic sampling unit of the study. Within each subplot, a Leica HDS6100 phase-shift Terrestrial Laser Scanner (TLS) was used to capture woodland canopy structure. The number and position of scan locations within a subplot was determined by the arrangement and density of canopy material in the subplot, with the aim to minimise shadows within the canopy, and to maximise canopy penetration. Between one and five scans were recorded per subplot, across all plots. Further information on the field setup of the TLS is presented in Table 1.

Five Leica 6" (15.24 cm) diameter planar tilt-and-turn cross-pattern reflective targets were located in each subplot to facilitate alignment of scans (Figure 2). The five targets were located roughly in a quincunx pattern, with one target at the subplot centre and the remaining four targets arranged in a cross pattern around the edges of the subplot, ensuring that all scans could see all five targets. To facilitate alignment of scans among subplots, the location of each target in real space was recorded using a Leica VIVA GS10 GNSS (Global Navigation Satellite Systems) unit (Figure 3). The GNSS was set up in a Post-Processing Kinematic (PPK) configuration with a base-station located ~ 100 m from the edge of each 1 ha plot with an unobstructed view of the sky hemisphere where possible. The location of each target was measured for at least four minutes to minimise measurement error (Figure 4).

30 3 Hemispherical photography field setup

To validate TLS canopy closure estimates, at the centre of each subplot a single photograph was taken with a full-frame DSLR camera, equipped with a circular fisheye lens. Further information on the hemispherical photography setup is presented in Table 2.

The fisheye lens had an equisolid (equal area) projection, with a projection function given by:

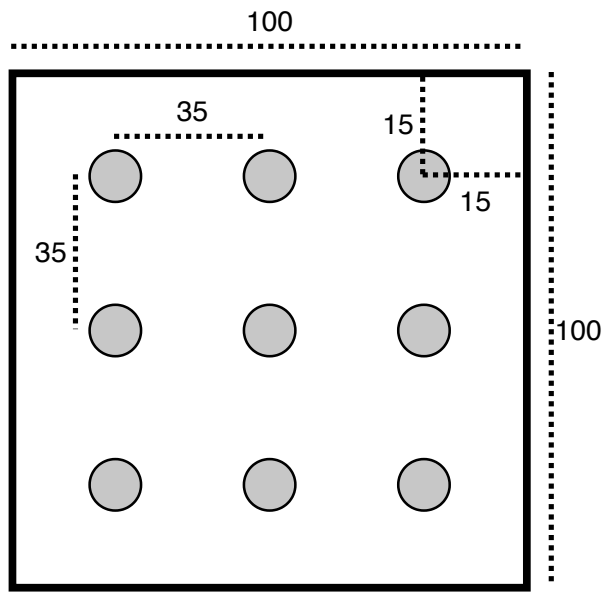


Figure 1: The layout of 10 m diameter subplots within each 1 ha plot. Each subplot is situated inside a 15 m buffer from the plot edge, with 35 m between subplot centres. Subplots are arranged in a 3×3 grid. All distances are in metres.



(a)



(b)

Figure 2: Example of a Leica 6" diameter reflective target, (a) in situ mounted on a length of threaded bar, and (b) showing the cross pattern face of the target.



Figure 3: A Leica VIVA GS10 GNSS unit in the field, showing the antenna atop an aluminium pole, attached to the base station on the ground, and the rover terminal in the hand of a research assistant.

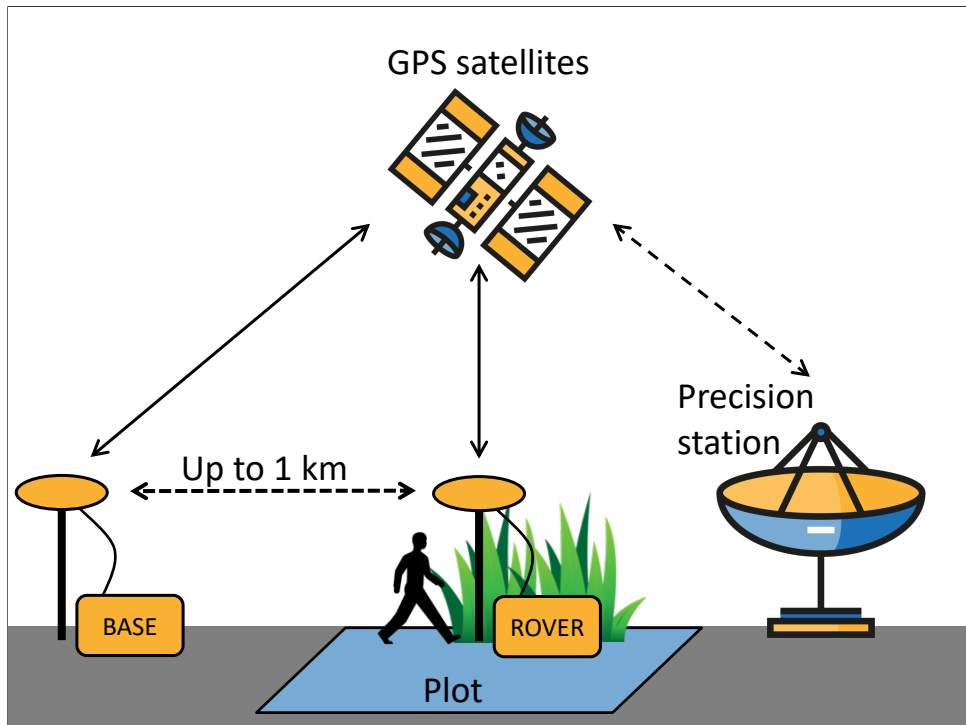


Figure 4: Schematic diagram of the GNSS PPK configuration used to precisely locate targets in real space. The base station is located in an area with a full unobstructed view of the sky hemisphere, up to ~1 km from the plot, and is left in the same location for the duration of the data collection, recording its location once per second. The rover is moved around inside the plot to record the location of each target, for >4 minutes at each target. The rover and the base station both utilise GPS and GLONASS satellites to record their position. After data collection, a two stage validation technique is used to improve the precision of the recorded positions, firstly using the base station, and secondly using the TrimbleRTX service which utilises highly precise distributed regional stations.

Table 1: Description of scan settings used for each scan.

Setting	Value
TLS model	Leica HDS6100
Wavelength	650-690 nm
Spot size at exit	3 mm
Beam divergence	0.22 mrad
Range	79 m @90%; 50 m @18% albedo
Azimuth range	0-360°
Zenith range	0-155°
Increment	0.018°
Point spacing over 25 m	7.9 mm
Pixels per line	20,000
Lines	10,000
Compressed file size	~800 MB
Duration of scan	6 minutes 44 seconds

$$R = 2f \sin\left(\frac{\theta}{2}\right) \quad (1)$$

35 Where R is the radial position of a point on the image, f is the focal length of the lens, and θ is
 36 the angle in radians of incident light on the lens. Equisolid lenses are preferred for hemispherical
 37 photography because they maintain an equal area for each pixel, i.e. a pixel projected through
 38 the lens has the same solid angle irrespective of the incident light angle, meaning that canopy
 39 closure estimations are not biased towards any part of the sky hemisphere (Herbert, 1987).

40 Photographs were taken facing directly to zenith using a camera-mounted spirit level, with
 41 the top of the camera body facing magnetic north, at a height of 1.3 m or above understorey
 42 vegetation, whichever was higher. Photographs were captured under uniform light conditions as
 43 much as possible, either under overcast skies or early in the day before direct sunlight could
 44 be seen on the photograph, to minimise lens flare, which can preclude accurate differentiation
 45 of plant material and sky, and to minimise ‘blooming’, a phenomenon where light ‘bleeds’ into
 46 dark areas of the image in highly contrasting light conditions (Frazer et al., 2001).

47 ImageJ (Fiji version 2.1.0/1.53c) was used to binarise hemispherical photographs, to separate
 48 plant material from sky (Schneider et al., 2012). Images were binarised using the Huang algorithm
 49 (Huang & Wang, 1995) using only the blue channel of the image, under the assumption that
 50 plant material reflects little blue light, while the sky reflects much more (Brusa & Bunker,
 51 2014). Images were saved as PNG files at the original pixel resolution, with a circular image of
 52 4016×4016 pixels.

53 4 Terrestrial LiDAR processing

54 4.1 Scan alignment and registration

55 Point clouds within a subplot were aligned using the reflective targets as anchor points. Point
 56 cloud alignment was conducted in Leica Cyclone (version 9.1) (Leica Camera AG, 2009).
 57 Reflective targets were manually located within each point cloud, then the precise centre of
 58 each target was identified automatically by Cyclone. Anchor points were discarded if they had

Table 2: Description of camera settings used for hemispherical photographs. Note that shutter speed and ISO are deliberately variable within sensible thresholds to allow adjustments for ambient light conditions.

Setting	Value
Camera model	Nikon D750
Lens model	Sigma 8 mm f/3.5 EX DG Circular Fisheye
Pixel pitch	5.95 μm
Sensor resolution	24.3 MP
Shutter speed	>1/60s
Aperture	5-7
ISO	100-200
Exposure compensation	-0.7 (Brusa & Bunker, 2014)
Focus	∞ (Hu & Zhu, 2009; Frazer et al., 2001)
Image size	Large Fine JPEG - circular image 4016×4016 px
Orientation	Landscape

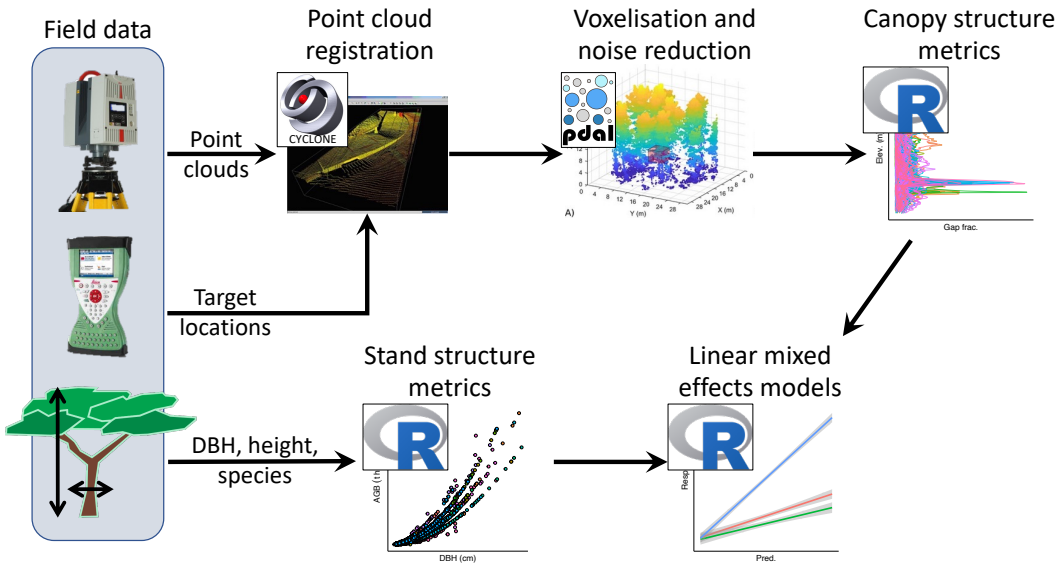


Figure 5: Schematic diagram summarising the data processing and analysis workflow for the TLS data. Processing steps are labelled according to the principal software used during that step.

Table 3: The five closes regional base stations to each site, used by TrimbleRTX to refine GNSS measurements

Site	Receiver	Distance (km)
Bicuar	JAVAD TRE 3	863
	JAVAD TRE 3 DELTA	1448
	TRIMBLE NETRS	1630
	TRIMBLE NETRS	1648
	JAVAD TRE G3TH DELTA	1796
Mtarure	SEPT POLARX5	686
	TRIMBLE ALLOY	795
	LEICA GRX1200GGPRO	903
	JAVAD TRE 3 DELTA	1119
	JAVAD TRE 3 DELTA	1315

59 a location uncertainty of >3 cm. After alignment, subplot point clouds were exported from
 60 Cyclone as PTX files for further processing.
 61 GNSS measurements of target locations were used to register point clouds in real space. The
 62 TrimbleRTX GNSS post-processing service was used to improve the precision of target locations
 63 recorded with GNSS, using distributed regional stations to validate the rover and base station
 64 GNSS measurements (Table 3) (Chen et al., 2011). Following point cloud registration, subplot
 65 point clouds were combined to a plot level point cloud.
 66 PTX files were converted to compressed LAZ files using PDAL (PDAL Contributors, 2018), to
 67 reduce file size and speed up further processing. Code 1 contains the code used to transform
 68 PTX to LAZ.

```

1 # Get file name without extension
2 noext=${1%.ptx}
3
4 # Find the PTX scan array dimension header material
5 lines=$(grep -E -n '^.{1,10}$' $1 |
6   cut -f1 -d: |
7   awk 'NR%2!=0' |
8   tr '\n' ' ' |
9   sed 's/^([0-9])\s//g')
10
11 # Split PTX file into individual scans
12 csplit -f "$noext" -b "%d.ptx" $1 $lines
13
14 $ Find split files
15 ptxsplit=$(find . -type f -regex ".*/${noext}_[0-9].ptx")
16
17 # For each file:
18 for j in ${ptxsplit}; do
19   jnoext="${j%.ptx}"
20   matrix=$(head -n 10 $j | tail -4 | sed -r 's/0\s+?$/0.0/g' | dos2unix)
21   pdal pipeline ptx_laz.json --readers.text.filename=$j \
22     --filters.transformation.matrix="${matrix}" \
23     --writers.las.filename=${jnoext}.laz
24 done
25
26 # List LAZ files
27 lazsplit=$(find . -type f -regex ".*/${noext}_[0-9].laz")
28
29 # Merge LAZ files
30 pdal merge ${lazsplit} ${noext}.laz

```

Code 1: The processing chain used to convert Leica Cyclone PTX files to LAZ files, using PDAL, POSIX shell scripting, and common UNIX utilities. The `ptx_laz.json` JSON pipeline is shown in Code 2.

```

1 [
2   {
3     "type" : "readers.text",
4     "filename" : "input.txt",
5     "header" : "X Y Z I",
6     "skip" : 10
7   },
8   {
9     "type" : "filters.transformation",
10    "matrix" : "0 -1 0 1 1 0 0 2 0 0 1 3 0 0 0 1"
11  },
12  {
13    "type" : "writers.las",
14    "compression" : "true",
15    "minor_version" : "2",
16    "dataformat_id" : "0",
17    "forward" : "all",
18    "filename" : "output.laz"
19  }
20 ]

```

Code 2: The JSON pipeline used in Code 1 to convert PTX files to LAZ files, and applying a rotation matrix.

71 **4.2 Voxelisation**

72 Point clouds were voxelised to different voxel sizes depending on the application of the data. 5
73 cm^3 cubic voxels were used for subplot height profile estimation, while 50 cm^3 voxels were used
74 for whole plot canopy rugosity. Variation in voxel size reflects the spatial scale of each analysis,
75 and is bounded by the beam divergence of the TLS over longer distances (Grau et al., 2017).
76 Choosing voxels that are too small can result in pock-marked representations of surfaces that
77 are especially problematic when calculating larger scale canopy structure metrics such as canopy
78 top roughness, while voxels that are too large can result in an over-estimation of plant volume
79 when estimating canopy foliage density at the subplot scale, especially when foliage is clumped
80 (Seidel et al., 2012; Cifuentes et al., 2014). Voxels were classified as ‘filled’ if they intersected
81 one or more points.

82 **4.3 Noise reduction**

83 Outlier detection and noise reduction of point clouds was conducted in PDAL, using the
84 “statistical method” of `filters.outlier` (Rusu et al., 2008), with $k = 8$ (mean number of
85 neighbours), and $m = 1.96$ (outlier distance threshold multiplier, here approximating a 95%
86 confidence interval):

$$\begin{aligned}\bar{\mu} &= \frac{1}{N} \sum_{i=1}^N \mu_i \\ \sigma &= \sqrt{\frac{1}{N-1} \sum_{i=1}^N (\mu_i - \bar{\mu})^2} \\ t &= \mu + m\sigma \\ \text{with } outlier_i &= \begin{cases} \text{true,} & \text{if } \mu_i \geq t \\ \text{false,} & \text{otherwise} \end{cases}\end{aligned}\tag{2}$$

87 Where μ_i is the mean distance from point i to all k nearest neighbour points, N is the number
88 of points in the scene, $\bar{\mu}$ is the mean distance to nearest neighbour points, σ is the standard
89 deviation of these mean distances, t is the threshold distance used to define an outlier and
90 $outlier_i$ is the condition of a point in the scene being identified as an outlier.

91 **4.4 Foliage density profiles**

92 To calculate subplot foliage density profiles, the 5 cm^3 voxelised point cloud was first cropped to
93 a 10 m diameter cylinder of infinite height. Ground points were identified using `filters.pmf`
94 (Progressive Morphological Filter - PMF) in PDAL (Zhang et al., 2003), and the height above
95 ground of all points was calculated using `filters.hag_nn` (Nearest Neighbour) in PDAL. Points
96 below ground level and above the 99th percentile of height were excluded from further analyses.
97 Height profile points were exported to XYZ coordinates then imported into R for further
98 processing.
99 In R, foliage density was calculated in 5 cm layers as the proportion of filled 5 cm^3 voxels. A
100 loess model with a span of 0.1 was fitted to the foliage density values in each layer to estimate
101 the foliage density profile (Figure 7). The foliage density profile was further filtered to only tree
102 canopy material, by discarding all points below 1.3 m.

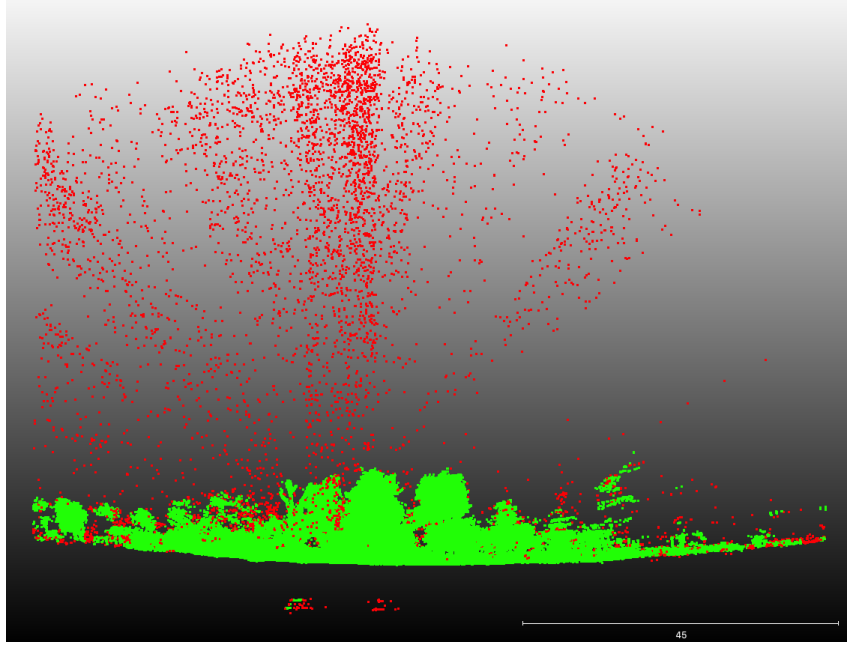


Figure 6: A 2 m deep cross section of a subplot point cloud showing the efficacy of the noise reduction and voxelisation process. Red points are excluded by the process, while green points are preserved for further analysis.

¹⁰³ 5 Subplot canopy complexity metrics

¹⁰⁴ 5.1 Effective Number of Layers

¹⁰⁵ The Effective Number of Layers (ENL) in the foliage density profile was used to estimate canopy
¹⁰⁶ structural complexity, using the true-numbers equivalent Shannon entropy of foliage density
¹⁰⁷ among 50 cm vertical layers (Ehbrecht et al., 2016):

$$\text{ENL} = \exp \left(- \sum_{i=1}^N p_i \times \ln p_i \right) \quad (3)$$

¹⁰⁸ Where N is the number of 50 cm bins in the height profile, and p_i is the proportion of filled
¹⁰⁹ voxels in layer i (foliage density). While Ehbrecht et al. (2016) used 1 m layers, their study was
¹¹⁰ conducted in temperate deciduous forest where the maximum height of the sampled forest stands
¹¹¹ was 40 m, whereas the maximum canopy height in this study was only 22 m. Both Ehbrecht
¹¹² et al. (2016) and Montes et al. (2004) assert that the choice of layer thickness is largely arbitrary,
¹¹³ but should be determined with respect to the variability within the canopy, thus in the sparse
¹¹⁴ and highly variable savanna tree canopies measured in this study, narrower layers were chosen.

¹¹⁵ 5.2 Foliage density profile and uniformity

¹¹⁶ Subplot canopy foliage density was calculated as the area under the curve of the canopy foliage
¹¹⁷ density profile, using trapezoid estimation. To describe the uniformity of the foliage density
¹¹⁸ distribution through the canopy, a linear model of cumulative foliage volume vs. height was
¹¹⁹ fitted (Figure 7). Under a completely even distribution of foliage material through the canopy,
¹²⁰ the residuals of the linear model tend to zero, while clumping causes deviations from this uniform
¹²¹ distribution and increases the sum of squared residuals.

¹²² Maximum canopy height has been used in other studies to describe canopy structural complexity
¹²³ (Scheuermann et al., 2018). At the small spatial scale of the subplots used in this study however,
¹²⁴ there proved to be too much stochastic variation in canopy height among subplots due to
¹²⁵ the distribution of individual trees to make this statistic informative as a measure of canopy
¹²⁶ complexity. Canopy height was instead calculated later at the plot level.

¹²⁷ 5.3 Canopy closure

¹²⁸ Subplot canopy closure, i.e. the proportion of the sky hemisphere occluded by plant material,
¹²⁹ a.k.a. gap fraction or site factor (Jennings, 1999), was measured by simulating a hemispherical
¹³⁰ image at the centre of the subplot using the point cloud data from all scans per subplot. The
¹³¹ point cloud was first cropped to a 20 m diameter cylinder around the subplot centre using
¹³² PDAL. Points below 1.3 m and within a 50 cm sphere around the subplot centre at 1.3 m height
¹³³ were discarded, to prevent the simulated hemispherical image being occluded by understorey
¹³⁴ vegetation. POV-Ray was used to simulate the hemispherical image using ray-tracing (Persistence
¹³⁵ of Vision Pty. Ltd., 2004). Filled voxels were represented in POV-Ray as non-reflective black
¹³⁶ cubes filling the 5 cm³ voxel volume, with a white uniform sky box and no light source. POV-Ray
¹³⁷ produced an image with identical qualities to that of the real hemispherical photograph, using a
¹³⁸ fisheye lens with an equisolid projection and a view angle of 180°, located at the subplot centre
¹³⁹ at 1.3 m above the ground, with the top of the camera facing magnetic north and the camera
¹⁴⁰ facing directly to zenith, producing a circular image of 4016×4016 pixels.

¹⁴¹ Hemiphot (ter Steege, 2018) was used to estimate closure from both the hemispherical photo-
¹⁴² graphs and the TLS POV-Ray simulation. Images were cropped to a circle of 60° zenith angle.
¹⁴³ It can be supposed that below 60°, under most woodland canopies, variation in tree canopy
¹⁴⁴ density does little to affect sunlight penetration, due to the greater depth of canopy at these
¹⁴⁵ angles (Jupp et al., 2008). To obtain the total closure (C_α) of a circular image:

$$C_\alpha = 1 - G_{\text{tot}} = \sum_{\alpha=0.5}^{\alpha=60.0} (G_\alpha A_\alpha / A_{\text{tot}}) \quad (4)$$

¹⁴⁶ Where G_α is the fraction of unfilled pixels in ring α , A_α is the sky area of the ring segment, and
¹⁴⁷ A_{tot} is the total sky area of the hemisphere.

¹⁴⁸ Canopy closure estimates from the TLS were validated using estimates from hemispherical
¹⁴⁹ photography. A Pearson's correlation analysis showed that both methods were highly correlated
¹⁵⁰ ($r(195)=0.89$, $p<0.001$). TLS estimates of closure were almost exclusively higher than hemispherical
¹⁵¹ photography estimates, except in a few subplots with particularly low canopy closure. At
¹⁵² higher canopy closure the over-estimation of canopy closure by TLS was larger (Figure 8). This
¹⁵³ finding is in agreement with previous studies which have found that the magnitude of TLS
¹⁵⁴ canopy closure over-estimation depends on gap size distribution, where a site with greater canopy
¹⁵⁵ cover and a gap fraction dominated by small within crown gaps will have a larger over-estimate
¹⁵⁶ than a more open site with a gap fraction dominated by large between crown gaps (Seidel et al.,
¹⁵⁷ 2012). A linear mixed model which included nested random intercept effects for subplots within
¹⁵⁸ plots was used to identify if sites differed significantly in their relationship between hemispherical
¹⁵⁹ photography and TLS estimates of canopy closure. There was no significant difference in model
¹⁶⁰ fixed effect slope between plots in Bicuar National Park, Angola, and those in Mtarure, Tanzania
¹⁶¹ ($\beta(173)=0.13\pm0.0098$, $p=0.18$).

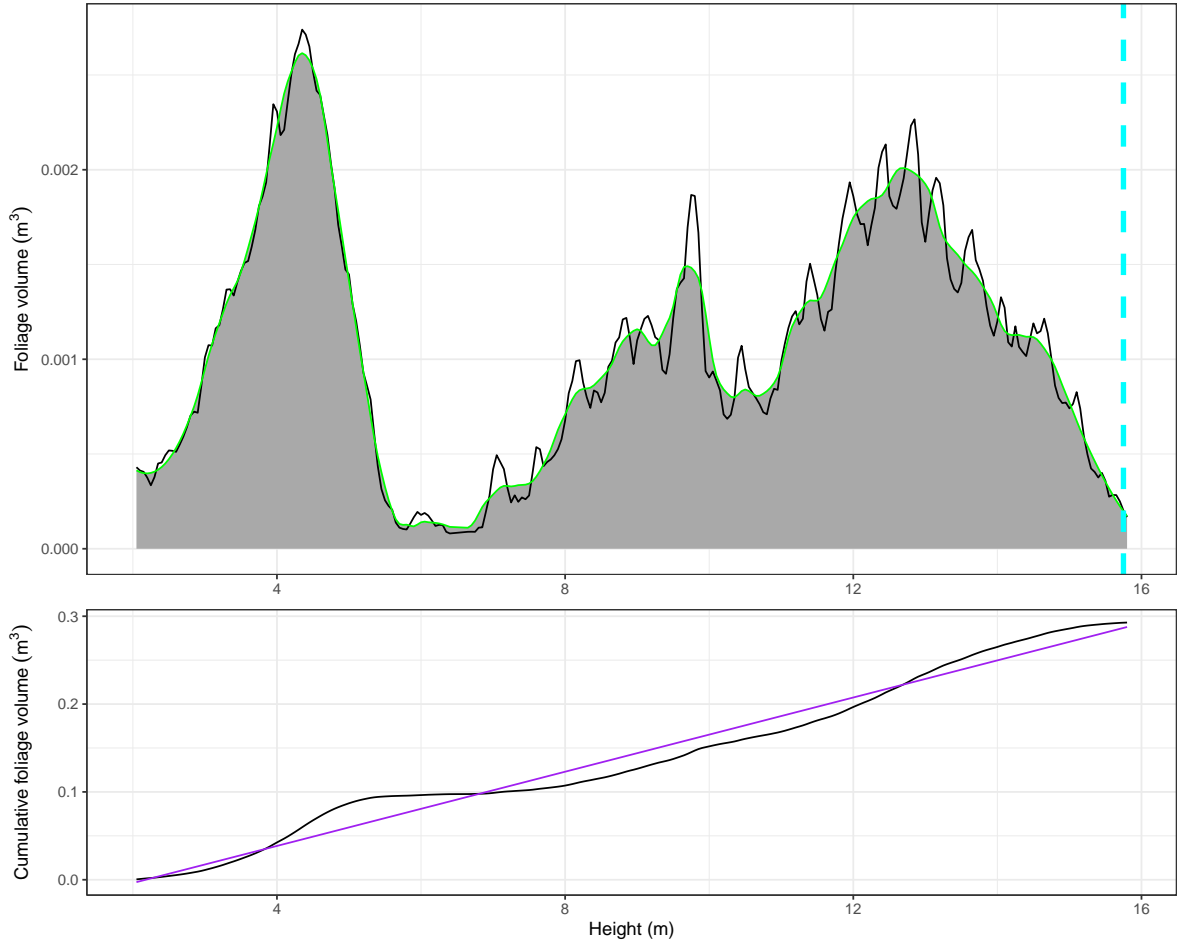


Figure 7: Subplot foliage volume height profile (top) and cumulative foliage volume profile (bottom) for a subplot in Bicuar National Park, Angola, to illustrate some of the canopy structure metrics extracted from each height profile. In the top panel: the dashed cyan line shows the 99th percentile of canopy height, used here as a measure of canopy top height in plot level canopy surface modelling. The black trace shows the foliage density height profile, and the green trace shows the loess model fitted to the data, with the area under the canopy shaded grey. The bottom panel: the black trace shows the cumulative foliage volume through the canopy, taken from the loess fit in the top panel. The purple line shows the line of best fit of a linear model through this data. Not illustrated is the Effective Number of Layers (ENL) metric.

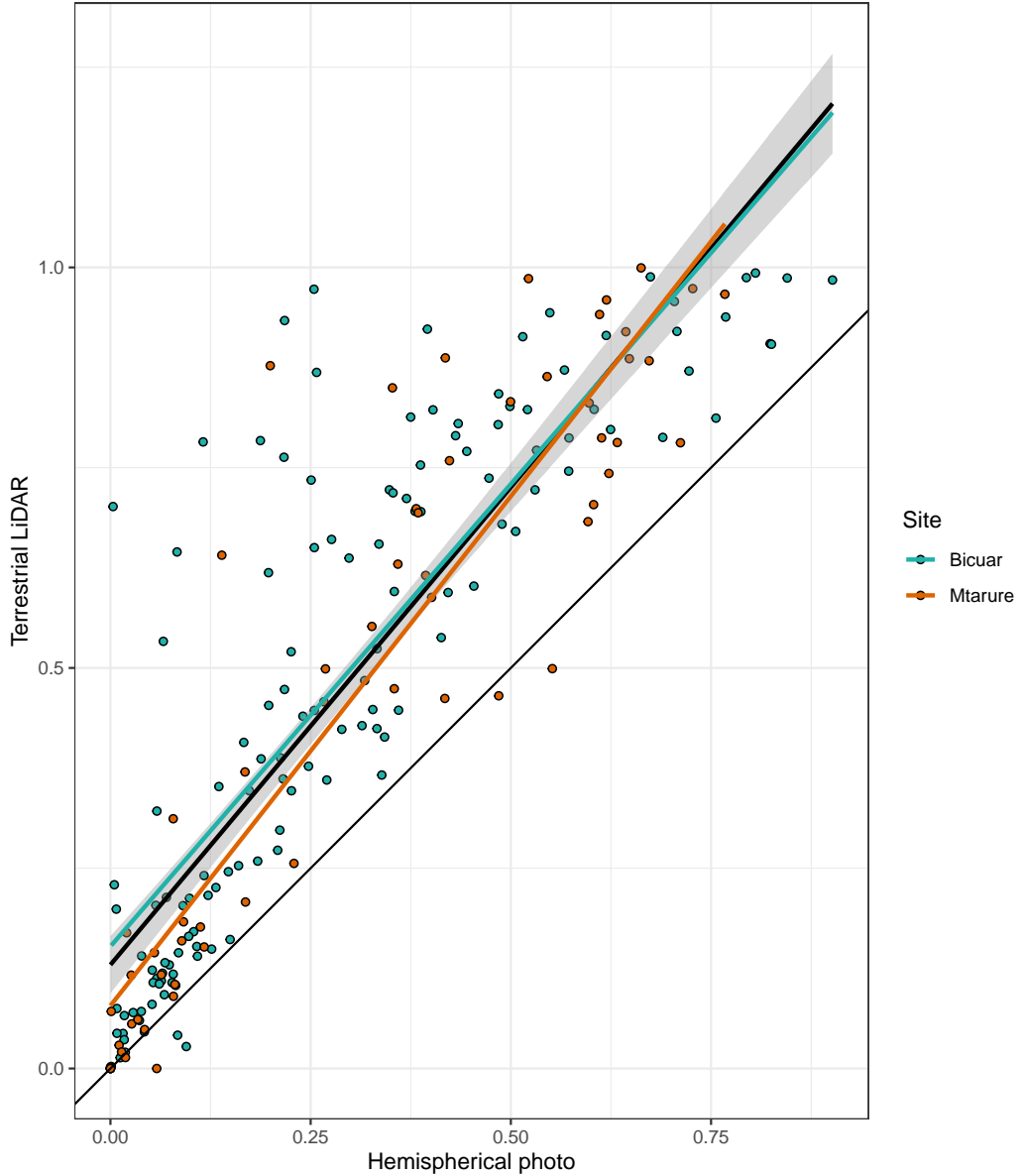
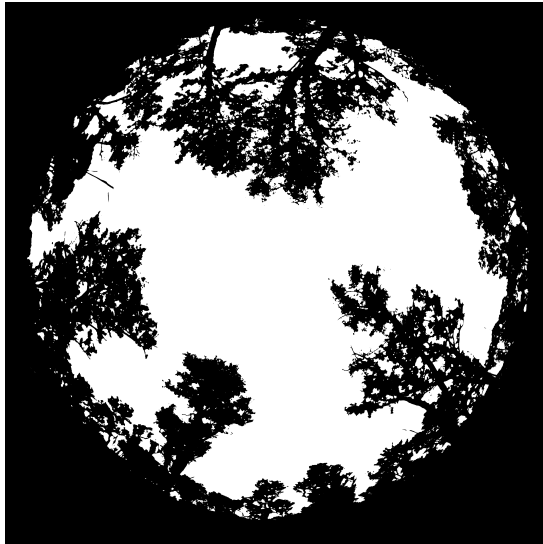


Figure 8: Comparison of canopy closure estimation from TLS and hemispherical photography. The thick black line of best fit is a linear model of all points ± 1 standard error, while the coloured lines are site specific linear models. The thin black line shows the 1:1 fit.



(a)



(b)

Figure 9: Comparison of hemispherical images for a subplot in Bicuar National Park, Angola. (a) A hemispherical photograph, and (b) a multi-scan point cloud modelled as cubic voxels with POV-Ray. The hemispherical photograph (left) shows some blooming, especially in the tree on the bottom right of the image, where light is seen ‘bleeding’ through the darker canopy material, causing an under-estimation in canopy closure. Note also that while there are minor variations in image height between TLS and hemispherical photos, this does not affect canopy closure estimates, as images were first cropped to a 60° angle of view.

162 6 Whole plot canopy complexity metrics

163 6.1 Canopy height

164 The canopy height of each 1 ha plot was estimated using unified point clouds from all subplots.
165 The unified point cloud was voxelised to 10 cm^3 , and the 99th percentile of height was recorded
166 as the canopy height of each 10 cm^2 column. Maximum height was not used as this occasionally
167 constituted a severe outlier which skewed further canopy surface model smoothing. The point
168 cloud was then cropped to the plot boundaries, located using PPK GNSS similar to the TLS
169 targets. A pit-filling algorithm described in Khosravipour et al. (2014) was used to smooth the
170 canopy surface model, at a resolution of 50 cm, removing gaps within trees caused by incomplete
171 penetration of the LiDAR beam (Figure 10).

172 Mean canopy height across the plot and the coefficient of variation of canopy height were
173 extracted from the canopy surface model for use in statistical analyses. The coefficient of
174 variation of canopy height describes canopy structural diversity measured by the heterogeneity
175 of the canopy surface (Parker & Russ, 2004). Other studies in closed canopy temperate and
176 boreal forests have used metrics similar to the Topographic Roughness Index to measure canopy
177 surface heterogeneity, by comparing canopy height to that of neighbouring pixels in the canopy
178 height model (Weligepolage et al., 2012; Herrero-Huerta et al., 2020). In this study however, the
179 sparse nature of the tree canopies meant that these metrics were overly influenced by canopy
180 density and the edges of individual tree canopies.

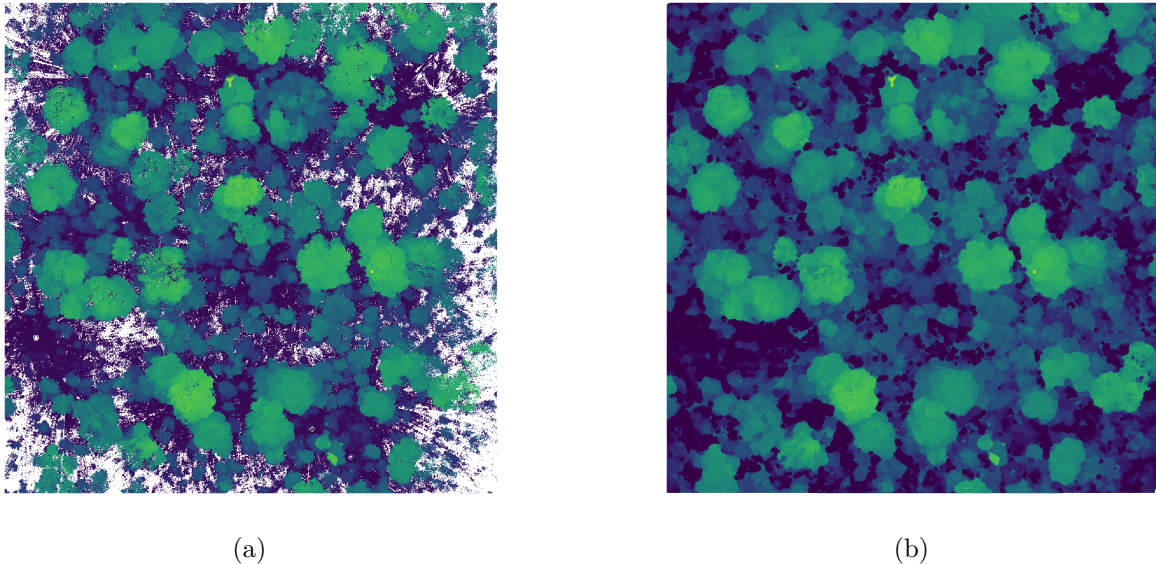


Figure 10: Top-down view of a 1 ha plot in Bicuar National Park. (a) The point cloud after voxelisation, noise reduction, and taking the 99th percentile of stem height in each 5 cm vertical bin. (b) The same point cloud after pit filling to generate a smooth canopy height profile. Points are coloured according to point height from the ground.

181 6.2 Canopy rugosity and foliage density

182 Canopy rugosity (R_c) was calculated to describe structural complexity across the entire canopy
183 profile of each plot, rather than just the canopy surface (Hardiman et al., 2011). R_c first
184 calculates the standard deviation of foliage density in 50 cm^2 columns across the plot (σG_z),
185 then calculates the standard deviation of those standard deviations:

$$R_c = \sigma(\sigma G_z)_x \quad (5)$$

186 Where G_z is the vertical height axis z , x is the horizontal axis, and σ is the standard deviation.
187 Additionally, foliage density was calculated at the plot level as the sum of filled 50 cm^3 voxels
188 across the plot, and plot canopy closure was calculated as the mean of all subplot canopy closure
189 estimates.

190 7 Stand structure metrics

191 7.1 Spatial mingling of species

192 The spatial mingling index (M_i) is a spatially explicit estimate of the degree to which species are
193 spatially mixed within a plot. Here, M was calculated at the plot level as the mean of M_i (von
194 Gadow & Hui, 2002), with the adjustment for potential neighbourhood species pool suggested
195 by Hui et al. (2011):

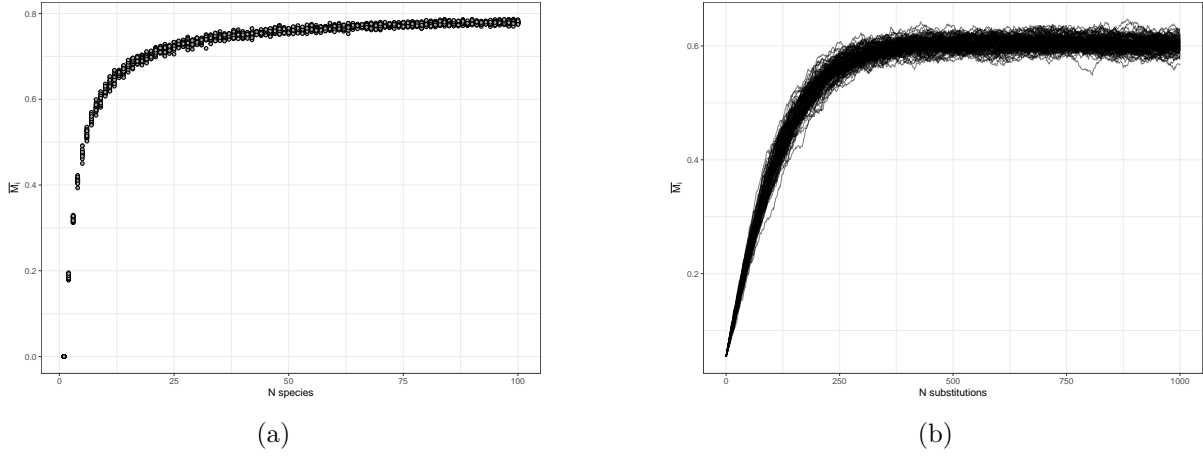


Figure 11: The behaviour of the spatial mingling index (M_i) with increasing number of species (a), and increasing spatial mixing of species (b). The left panel was generated by randomly assigning different numbers of species, in equal proportions, to an evenly spaced grid of individuals. 20 replicates were conducted for each number of species. The right panel was generated by randomly swapping pairs of individuals in a plot with 9 species arranged in mono-specific square blocks in an evenly spaced grid. Each line shows a single replicate, where individuals were swapped in an additive fashion, with 100 total.

$$M = \bar{M}_i$$

$$M_i = \frac{S_i}{n_{\max}} \frac{1}{k} \sum_{j=1}^k v_j \quad (6)$$

with $v_j = \begin{cases} 0, & \text{neighbour } j \text{ same species as reference } i \\ 1, & \text{otherwise} \end{cases}$

Where k is the number of nearest neighbours considered for each reference tree, S_i is the number of species found among the k nearest neighbours of tree i , n_{\max} is the potential number of species in the neighbourhood, i.e. $k + 1$, and N is the total number of trees in the plot. The conventional value of $k = 4$ was used here (von Gadow & Hui, 2002; Hui & Albert, 2004; Hui et al., 2007). The value of M_i increases with greater mixing of species, and all else being equal will increase with number of species within the plot (Figure 11).

7.2 Uniform angle index

The uniform angle index (winkelmass, W) was calculated to estimate the degree of spatial regularity in stem spatial distribution. Here, W was calculated at the plot level as the mean of W_i (von Gadow & Hui, 2002):

$$W = \bar{W}_i$$

$$W_i = \frac{1}{k} \sum_{j=1}^k v_j \quad (7)$$

with $v_j = \begin{cases} 0, & \alpha_j \leq \alpha_0 \\ 1, & \text{otherwise} \end{cases}$

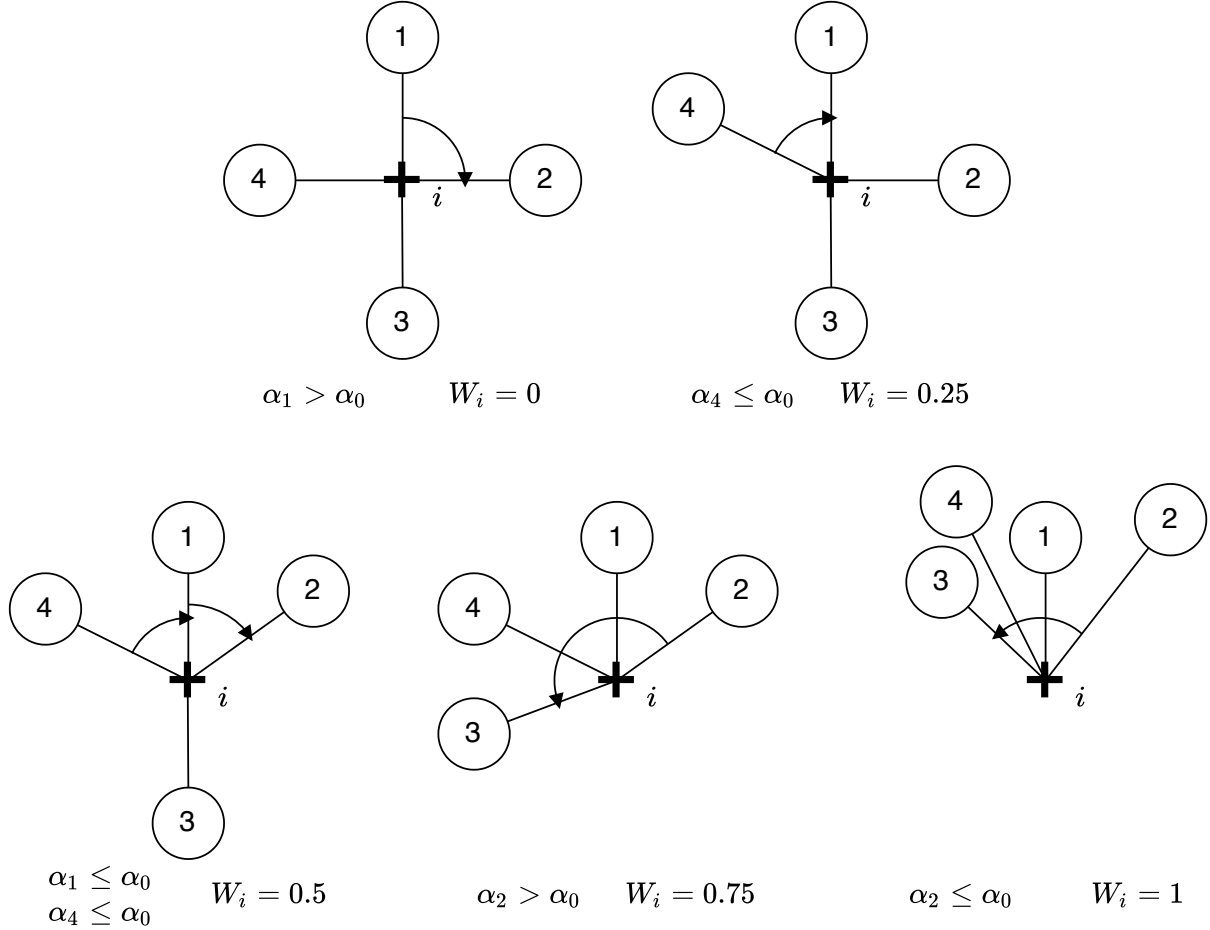


Figure 12: Possible values of W_i at a sample point i , denoted by a cross. Neighbours are represented as circles numbered sequentially from 1 to 4, where $k = 4$. The angles of arrows in each example are given below, along with the uniform angle index for that example.

206 Where k is the number of neighbours considered, α_j is the angle between consecutive neighbours
 207 and α_0 is the critical angle, where $\alpha_0 = 72^\circ$ (Hui & Gadow, 2002). Figure 12 demonstrates
 208 how the value of W_i varies according to spatial distribution of neighbours. The value of the
 209 uniform angle index increases with increasing spatial clumping (decreasing spatial regularity)
 210 of individuals (Figure 13), and in a plot with random tree distribution will increase as more
 211 neighbours are considered (Figure 14).

212 7.3 Voronoi tessellation

213 In addition to spatial regularity, the spatial uniformity of stems is another important aspect
 214 of tree spatial distribution. While the uniform angle index effectively measures similarity to a
 215 grid-like distribution of individuals, it does not account for variation in the relative distance of
 216 stems from their neighbours over the plot area. Spatial uniformity is defined here by two criteria:
 217 equality of spacing among individuals within the plot, and even coverage of individuals across
 218 the plot (Ong et al., 2012). Departures from spatial uniformity indicate clustering of individuals.
 219 Voronoi tessellation is a method of partitioning an n -dimensional space into regions according to
 220 the closest individual (Figure 15). Voronoi tessellation was conducted using stem location within
 221 each plot. The coefficient of variation of the area of Voronoi cells was then used as a measure
 222 of spatial clustering which is sensitive to both the criteria defining spatial uniformity, and is

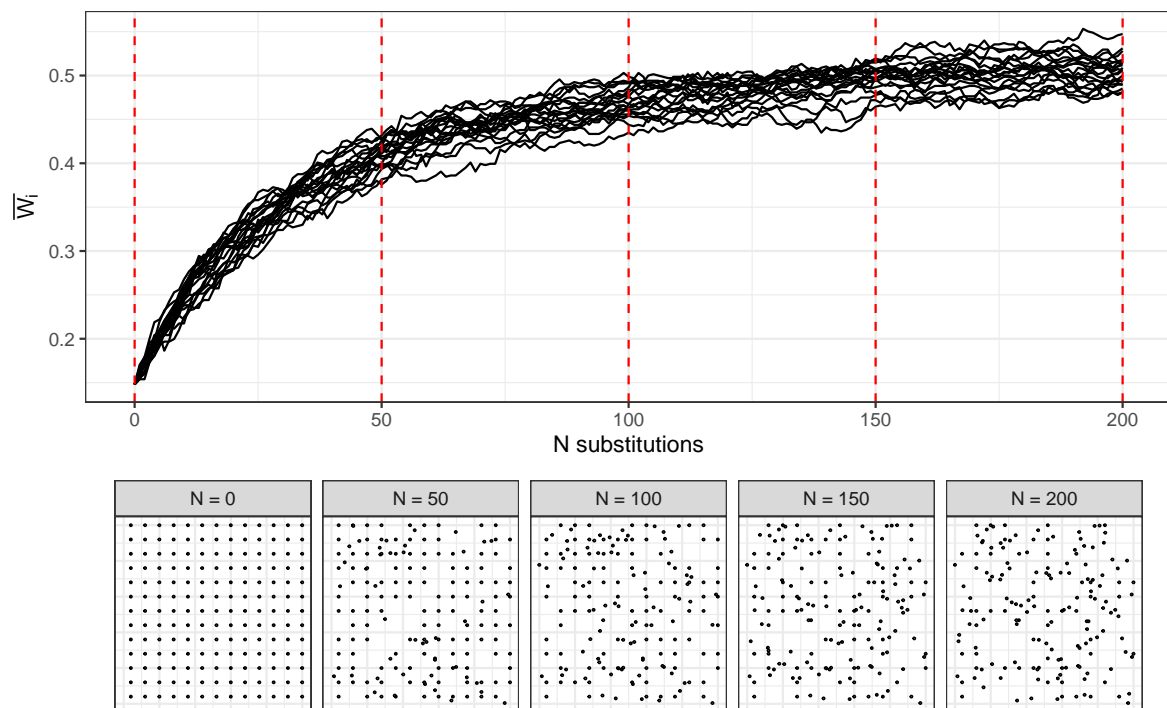


Figure 13: Variation in uniform angle index with increasing spatial irregularity of individuals. The top panel shows variation of uniform angle index in 20 plots as individuals are sequentially moved to a random location within the plot. Red dotted lines correspond to the panels below which show the spatial distribution of individuals after a given number of random individual movements.

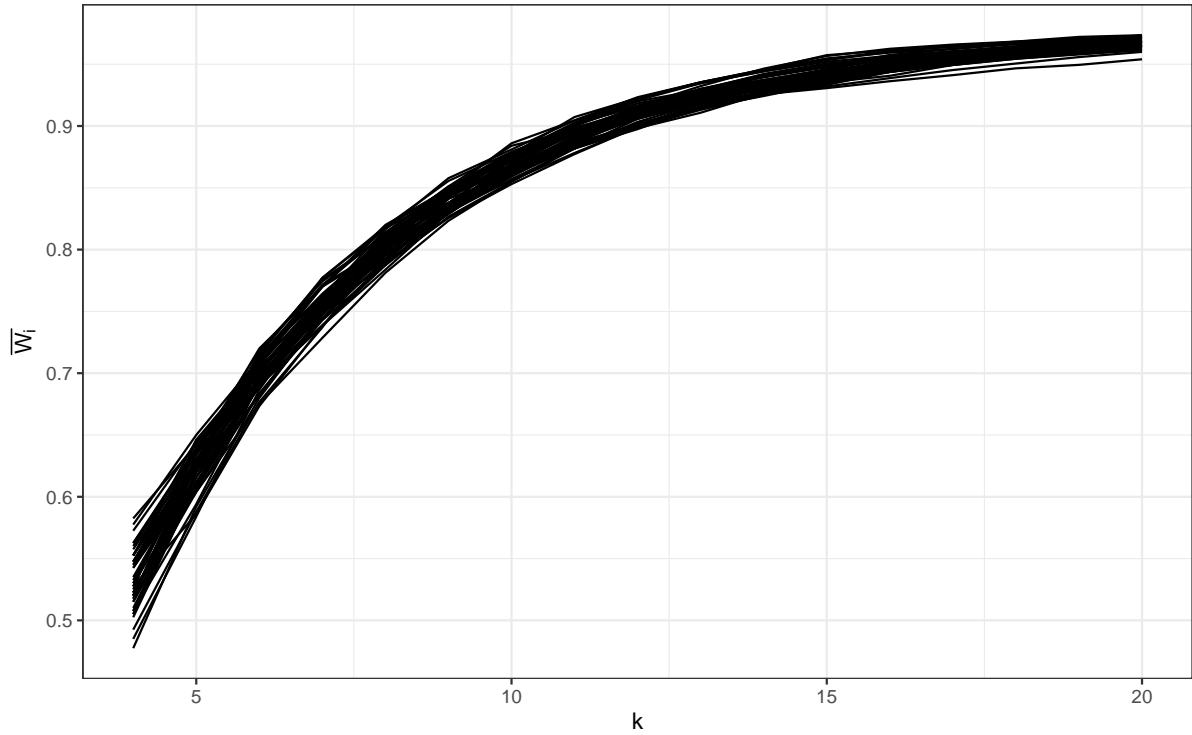


Figure 14: Variation in uniform angle index with increasing number of neighbours k considered in the calculation. 50 replicate plots were used, each with 100 individuals randomly distributed in space.

223 independent of tree density (Figure 16). As clustering increases, individuals within clusters will
 224 exhibit progressively smaller Voronoi cells, while individuals at the edges of clusters will exhibit
 225 progressively larger Voronoi cells, thus increasing the coefficient of variation of cell area.

226 7.4 Subplot canopy crowding

227 An adapted version of the Iterative Hegyi Index (H_i) was used to estimate tree spatial structure
 228 in subplots (Hegyi, 1974). The adapted formula used here allows the index to be based on a point
 229 rather than a focal tree, transforming it from a tree-centric competition index to a point-centric
 230 crowding index:

$$H_i = \log \sum_{j=1}^n \left(\frac{1}{L_{ij}} D_j \right) \quad (8)$$

231 Where n is the number of stems with canopy material within the subplot, D_j is the stem diameter
 232 of stem j and L_{ij} is the distance of stem j from the subplot centre i . H_i uses an iterative method
 233 for choosing active canopy occupants at the subplot centre, where the nearest individual to the
 234 subplot centre from each of 12 equally sized sectors is classified as the active stem (Figure 17).
 235 H_i was preferred over stem density to describe stem crowding in subplots because it is sensitive
 236 to how close a stem is to the subplot centre, which will affect canopy closure even if the number
 237 of stems in the subplot remains the same.

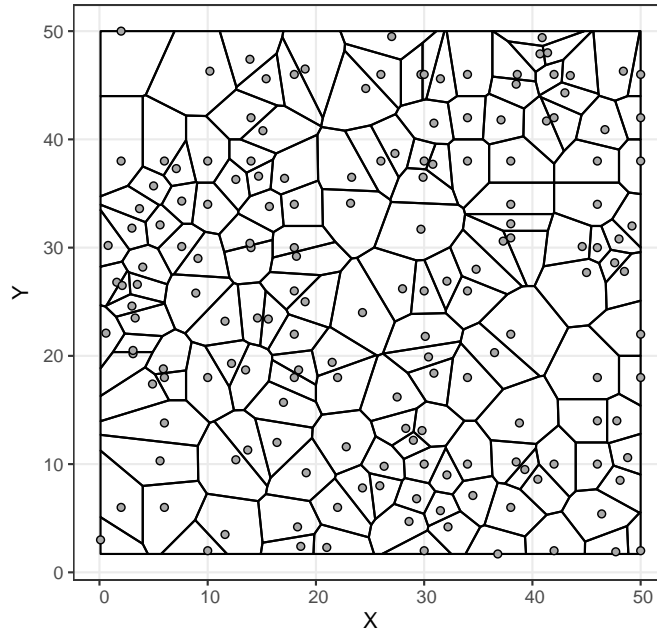


Figure 15: An example of a square plot with 100 randomly located individuals, with polygons constructed by Voronoi tessellation.

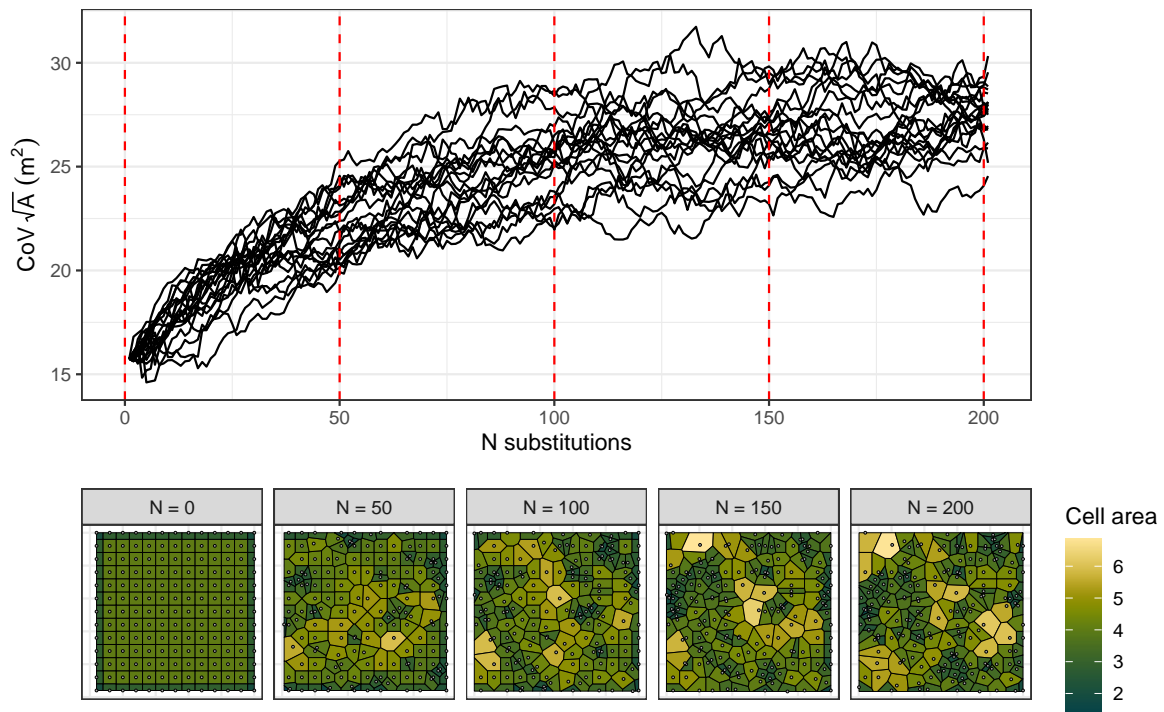


Figure 16: The coefficient of variation of Voronoi cell area with increasing spatial irregularity of individuals. The top panel shows variation in coefficient of variation of Voronoi cell area in 20 plots as individuals are sequentially moved to a random location within the plot. Red dotted lines correspond to the panels below which show the spatial distribution of individuals after a given number of random individual movements. Voronoi cells in the bottom panels are shaded according to their area.

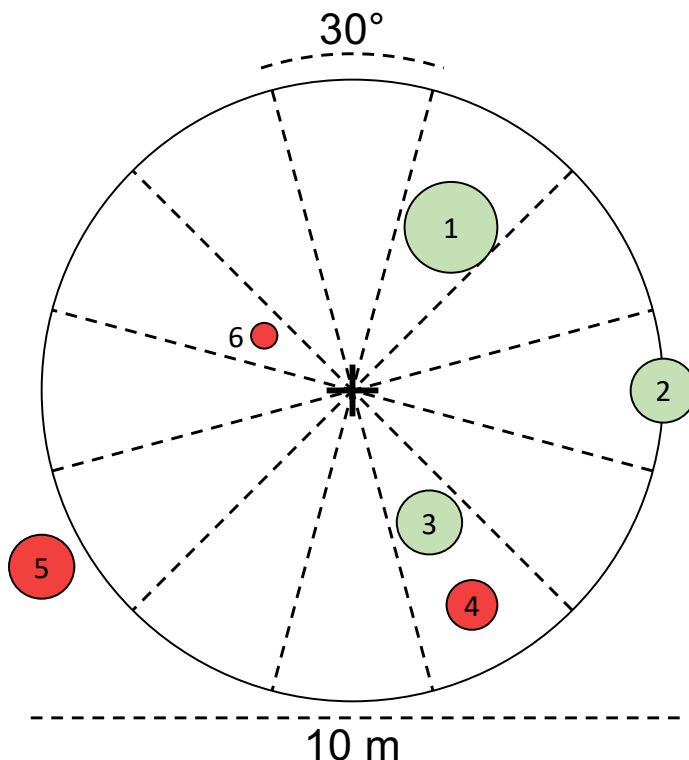


Figure 17: Schematic diagram demonstrating use of the Iterative Hegyi Index to assess crowding within each subplot. The 10 metre diameter subplot is divided into 12 equally sized sectors. Within each sector, the nearest stem of sufficient size (>5 cm diameter) to the subplot centre is recorded (e.g. 1). All stems with any canopy material inside the subplot are valid (e.g. 2). Stem 4 is not valid as it is behind stem 3. Stem 5 is invalid as all its canopy is outside the subplot. Stem 6 is too small to be recorded.

238 References

- 239 Brusa, A. & D. E. Bunker (2014). 'Increasing the precision of canopy closure estimates from
240 hemispherical photography: Blue channel analysis and under-exposure'. In: *Agricultural and
241 Forest Meteorology* 195-196, pp. 102–107. DOI: 10.1016/j.agrformet.2014.05.001.
- 242 Chen, X., T. Allison, W. Cao, K. Ferguson, S. Grunig, V. Gomez, A. Kipka, J. Kohler, H.
243 Landau, R. Leandro et al. (2011). *Trimble RTX, an innovative new approach for network
244 RTK*. Tech. rep. Portland OR, USA: International Technical Meeting of the Satellite Division
245 of the Institute of Navigation, ION GNSS, pp. 2214–2219.
- 246 Cifuentes, R., D. V. der Zande, J. Farifteh, C. Salas & P. Coppin (2014). 'Effects of voxel size
247 and sampling setup on the estimation of forest canopy gap fraction from terrestrial laser
248 scanning data'. In: *Agricultural and Forest Meteorology* 194, pp. 230–240. DOI: 10.1016/j.
249 agrformet.2014.04.013.
- 250 Ehbrecht, M., P. Schall, J. Juchheim, C. Ammer & D. Seidel (2016). 'Effective number of layers:
251 A new measure for quantifying three-dimensional stand structure based on sampling with
252 terrestrial LiDAR'. In: *Forest Ecology and Management* 380, pp. 212–223. DOI: 10.1016/j.
253 foreco.2016.09.003.
- 254 Frazer, G. W., R. A. Fournier, J. Trofymow & R. J. Hall (2001). 'A comparison of digital and
255 film fisheye photography for analysis of forest canopy structure and gap light transmission'. In:
256 *Agricultural and Forest Meteorology* 109.4, pp. 249–263. DOI: 10.1016/s0168-1923(01)00274-
257 x.
- 258 Grau, E., S. Durrieu, R. Fournier, J.-P. Gastellu-Etchegorry & T. Yin (2017). 'Estimation
259 of 3D vegetation density with Terrestrial Laser Scanning data using voxels. A sensitivity
260 analysis of influencing parameters'. In: *Remote Sensing of Environment* 191, pp. 373–388. DOI:
261 10.1016/j.rse.2017.01.032.
- 262 Hardiman, B. S., G. Bohrer, C. M. Gough, C. S. Vogel & P. S. Curtis (2011). 'The role of canopy
263 structural complexity in wood net primary production of a maturing northern deciduous
264 forest'. In: *Ecology* 92.9, pp. 1818–1827. DOI: 10.1890/10-2192.1.
- 265 Hegyi, F. (1974). 'A simulation model for managing jack-pine stands'. In: *Royal College of
266 Forestry, editor*. Stockholm, Sweden: Royal College of Forestry, pp. 74–90.
- 267 Herbert, T. J. (1987). 'Area projections of fisheye photographic lenses'. In: *Agricultural and
268 Forest Meteorology* 39.2-3, pp. 215–223. DOI: 10.1016/0168-1923(87)90039-6.
- 269 Herrero-Huerta, M., A. Bucksch, E. Puttonen & K. M. Rainey (2020). 'Canopy Roughness: A
270 New Phenotypic Trait to Estimate Aboveground Biomass from Unmanned Aerial System'. In:
271 *Plant Phenomics* 2020, pp. 1–10. DOI: 10.34133/2020/6735967. URL: <https://doi.org/10.34133%2F2020%2F6735967>.
- 272 Hu, L. & J. Zhu (2009). 'Determination of the tridimensional shape of canopy gaps using two
273 hemispherical photographs'. In: *Agricultural and Forest Meteorology* 149.5, pp. 862–872. DOI:
274 10.1016/j.agrformet.2008.11.008.
- 275 Huang, L. & M. J. Wang (1995). 'Image thresholding by minimizing the measures of fuzziness'.
276 In: *Pattern Recognition* 28.1, pp. 41–51. DOI: 0031-3203/95.
- 277 Hui, G. & M. Albert (2004). 'Stichprobensimulationen zur Schätzung nachbarschaftsbezogener
278 Strukturparameter in Waldbeständen [Simulation studies for estimating neighborhood-based
279 structural parameters in forest stands]'. In: *Allgemeine Forst und Jagdzeitung* 175, pp. 10–11.
- 280 Hui, G., K. von Gadow, Y. Hu & H. Xu (2007). *Structure-based forest management*. Beijing,
281 China: China Forestry Publishing House.
- 282 Hui, G., X. Zhao, Z. Zhao & K. von Gadow (2011). 'Evaluating tree species spatial diversity
283 based on neighbourhood relationships'. In: *Forest Science* 57.4, pp. 292–300. DOI: 10.1093/
284 forestscience/57.4.292.
- 285 Hui, G. & K. Gadow (2002). 'Das Winkelmaß-Theoretische Überlegungen zum optimalen
286 Standardwinkel'. In: *Allgemeine Forst U. Jagdzeitung* 173 (9), pp. 173–177.

- 288 Jennings, S. (1999). ‘Assessing forest canopies and understorey illumination: canopy closure,
289 canopy cover and other measures’. In: *Forestry* 72.1, pp. 59–74. DOI: 10.1093/forestry/72.
290 1.59.
- 291 Jupp, D. L. B., D. S. Culvenor, J. L. Lovell, G. J. Newnham, A. H. Strahler & C. E. Woodcock
292 (2008). ‘Estimating forest LAI profiles and structural parameters using a ground-based laser
293 called ‘Echidna’’. In: *Tree Physiology* 29, pp. 171–181. DOI: 10.1093/treephys/tpn022.
- 294 Khosravipour, A., A. K. Skidmore, M. Isenburg, T. Wang & Y. A. Hussin (2014). ‘Generating
295 Pit-free Canopy Height Models from Airborne LiDAR’. In: *Photogrammetric Engineering &*
296 *Remote Sensing* 80.9, pp. 863–872. DOI: 10.14358/pers.80.9.863.
- 297 Leica Camera AG (2009). *Leica Cyclone*. Version 9.1.
- 298 Montes, F., I. Cañellas, M. del Río, R. Calama & G. Montero (2004). ‘The effects of thinning
299 on the structural diversity of coppice forests’. In: *Annals of Forest Science* 61.8, pp. 771–779.
300 DOI: 10.1051/forest:2004074.
- 301 Ong, M. S., Y. C. Kuang & M. P.-L. Ooi (2012). ‘Statistical measures of two dimensional
302 point set uniformity’. In: *Computational Statistics & Data Analysis* 56.6, pp. 2159–2181. DOI:
303 10.1016/j.csda.2011.12.005.
- 304 Parker, G. G. & M. E. Russ (2004). ‘The canopy surface and stand development: assessing
305 forest canopy structure and complexity with near-surface altimetry’. In: *Forest Ecology and*
306 *Management* 189.1-3, pp. 307–315. DOI: 10.1016/j.foreco.2003.09.001.
- 307 PDAL Contributors (2018). *PDAL Point Data Abstraction Library*. DOI: 10.5281/zenodo.
308 2556738.
- 309 Persistence of Vision Pty. Ltd. (2004). *Persistence of Vision Raytracer (Version 3.7)*. [Computer
310 software].
- 311 Rusu, R. B., Z. C. Marton, N. Blodow, M. Dolha & M. Beetz (2008). ‘Towards 3D Point cloud
312 based object maps for household environments’. In: *Robotics and Autonomous Systems* 56.11,
313 pp. 927–941. DOI: 10.1016/j.robot.2008.08.005.
- 314 Scheuermann, C. M., L. E. Nave, R. T. Fahey, K. J. Nadelhoffer & C. M. Gough (2018).
315 ‘Effects of canopy structure and species diversity on primary production in upper Great
316 Lakes forests’. In: *Oecologia* 188.2, pp. 405–415. DOI: 10.1007/s00442-018-4236-x. URL:
317 <https://doi.org/10.1007%2Fs00442-018-4236-x>.
- 318 Schneider, C. A., W. S. Rasband & K. W. Eliceiri (2012). ‘NIH Image to ImageJ: 25 years of
319 image analysis’. In: *Nature Methods* 9.7, pp. 671–675. DOI: 10.1038/nmeth.2089.
- 320 Seidel, D., S. Fleck & C. Leuschner (2012). ‘Analyzing forest canopies with ground-based
321 laser scanning: A comparison with hemispherical photography’. In: *Agricultural and Forest
322 Meteorology* 154-155, pp. 1–8. DOI: 10.1016/j.agrformet.2011.10.006.
- 323 ter Steege, H. (2018). *Hemiphot.R: Free R scripts to analyse hemispherical photographs for
324 canopy openness, leaf area index and photosynthetic active radiation under forest canopies*.
325 Unpublished report. Leiden, The Netherlands: Naturalis Biodiversity Center. URL: <https://github.com/Naturalis/Hemiphot>.
- 326 von Gadow, K. & G. Hui (2002). ‘Characterising forest spatial structure and diversity’. In:
327 *Proceedings of the IUFRO International workshop ‘Sustainable forestry in temperate regions’*.
328 Ed. by L. Bjoerk. Lund, Sweden, pp. 20–30.
- 329 Weligepolage, K., A. Gieske & Z. Su (2012). ‘Surface roughness analysis of a conifer forest canopy
330 with airborne and terrestrial laser scanning techniques’. In: *International Journal of Applied
331 Earth Observation and Geoinformation* 14.1, pp. 192–203. DOI: 10.1016/j.jag.2011.08.014.
332 URL: <https://doi.org/10.1016%2Fj.jag.2011.08.014>.
- 333 Zhang, K., S.-C. Chen, D. Whitman, M.-L. Shyu, J. Yan & C. Zhang (2003). ‘A progressive
334 morphological filter for removing nonground measurements from airborne LiDAR data’. In:
335 *IEEE Transactions on Geoscience and Remote Sensing* 41.4, pp. 872–882. DOI: 10.1109/tgrs.
336 2003.810682.